

# Highly Reversible Ti/Sn Oxide Nanocomposite Electrodes for Lithium Ion Batteries Obtained by Oxidation of $\text{Ti}_3\text{Al}_{(1-x)}\text{Sn}_x\text{C}_2$ Phases

Irene Ostroman, Chiara Ferrara, Stefano Marchionna, Antonio Gentile, Nicholas Vallana, Denis Sheptyakov, Roberto Lorenzi, and Riccardo Ruffo\*

Among the materials for the negative electrodes in Li-ion batteries, oxides capable of reacting with  $\text{Li}^+$  via intercalation/conversion/alloying are extremely interesting due to their high specific capacities but suffer from poor mechanical stability. A new way to design nanocomposites based on the  $(\text{Ti}/\text{Sn})\text{O}_2$  system is the partial oxidation of the tin-containing MAX phase of  $\text{Ti}_3\text{Al}_{(1-x)}\text{Sn}_x\text{C}_2$  composition. Exploiting this strategy, this work develops composite electrodes of  $(\text{Ti}/\text{Sn})\text{O}_2$  and MAX phase capable of withstanding over 600 cycles in half cells with charge efficiencies higher than 99.5% and specific capacities comparable to those of graphite and higher than lithium titanate ( $\text{Li}_4\text{Ti}_5\text{O}_{12}$ ) or MXenes electrodes. These unprecedented electrochemical performances are also demonstrated at full cell level in the presence of a low cobalt content layered oxide and explained through an accurate chemical, morphological, and structural investigation which reveals the intimate contact between the MAX phase and the oxide particles. During the oxidation process, electroactive nanoparticles of  $\text{TiO}_2$  and  $\text{Ti}_{(1-y)}\text{Sn}_y\text{O}_2$  nucleate on the surface of the unreacted MAX phase which therefore acts both as a conductive agent and as a buffer to preserve the mechanical integrity of the oxide during the lithiation and delithiation cycles.

renewable energy sources necessarily require coupling with energy storage devices, not to mention the challenges of the development of efficient smart grids.<sup>[3]</sup> All these technologies rely on the use of safe, high-performance, and possibly low-cost batteries. Currently, the most widely used technology on the market is the lithium-ion battery (LIB), which is reliable and provides satisfying electrochemical performances.<sup>[4]</sup> However, the drawbacks of graphite (unsafe usage at high currents, aging), the most used negative electrode in LIBs, (theoretical capacity of  $\approx 370 \text{ mAh g}^{-1}$ ) are still pushing the research for materials that could give better performances. In this respect, a deeply investigated type of negative electrode is the family of MXenes, one of the most interesting intercalation materials, for the particular structure and electronic properties.<sup>[5–8]</sup> MXene compounds are a group of 2D lamellar materials described by the general formula  $\text{M}_{n+1}\text{X}_n\text{T}_x$ ,<sup>[9,10]</sup>

obtained from the etching of the corresponding MAX phase precursors, where M is a d-block transition metal, A is an element from the IIIA or IVA group, and X can be carbon or nitrogen. It can be found in the composition  $\text{M}_{n+1}\text{AX}_n$ , with  $n$  usually ranging from 1 to 3. MAX phases have layered hexagonal crystal structure (space group  $\text{P6}_3/\text{mmc}$ ) consisting of layers of  $\text{M}_6\text{X}$

## 1. Introduction

The need for electrochemical energy storage devices has become more and more crucial in the last decades. On one hand, the demand for portable electronics and electric vehicles has increased dramatically;<sup>[1,2]</sup> on the other hand, photovoltaics and other

I. Ostroman, C. Ferrara, N. Vallana, R. Lorenzi, R. Ruffo  
Dipartimento di Scienza dei Materiali  
Università degli Studi di Milano Bicocca  
Via Cozzi 55, Milano 20125, Italy  
E-mail: riccardo.ruffo@unimib.it

C. Ferrara, R. Ruffo  
National Reference Center for Electrochemical Energy Storage (GISEL)  
Via G. Giusti 9, Firenze 50121, Italy  
C. Ferrara, R. Ruffo  
INSTM  
Consorzio Interuniversitario per la Scienza e Tecnologia dei Materiali  
Via G. Giusti 9, Firenze 50121, Italy  
S. Marchionna, A. Gentile  
Ricerca sul Sistema Energetico – RSE S.p.A.  
Via R. Rubattino 54, Milano 20134, Italy  
D. Sheptyakov  
Paul Scherrer Institut  
Forschungsstrasse 111, Villigen PSI 5232, Switzerland

The ORCID identification number(s) for the author(s) of this article can be found under <https://doi.org/10.1002/smt.202300503>

© 2023 The Authors. Small Methods published by Wiley-VCH GmbH. This is an open access article under the terms of the Creative Commons Attribution-NonCommercial-NoDerivs License, which permits use and distribution in any medium, provided the original work is properly cited, the use is non-commercial and no modifications or adaptations are made.

DOI: 10.1002/smt.202300503

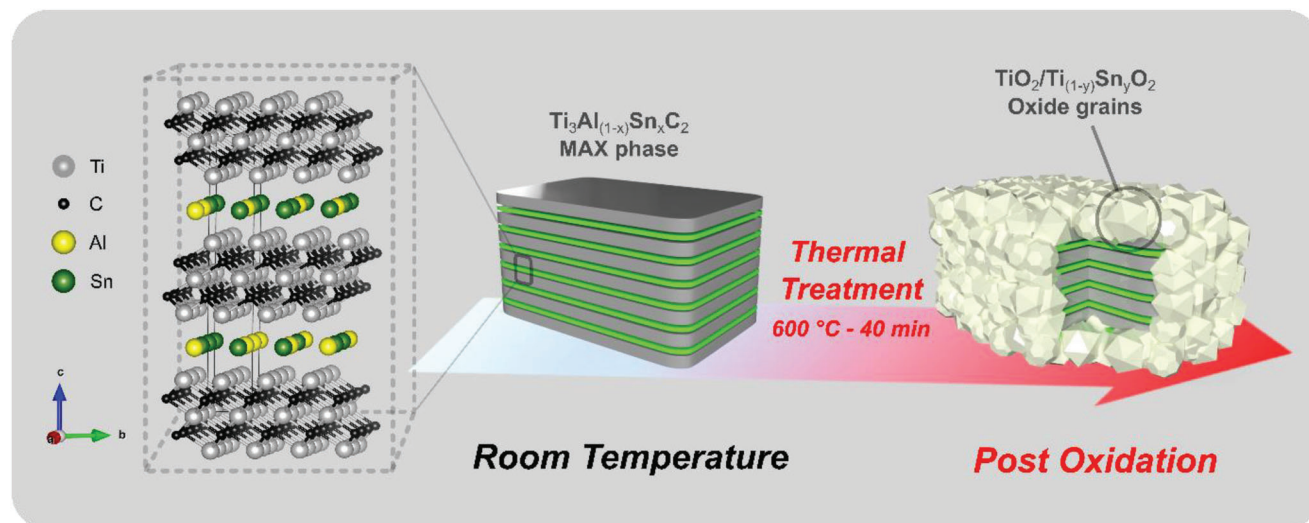


Figure 1. MAX phase crystal structure and scheme of the materials before and after the thermal treatment.

octahedra, with the X-atoms filling the octahedral sites, alternated with layers of pure A-elements along the *c* cell parameter<sup>[11]</sup> (see Figure 1). As found in the literature, one of the most studied MAX phase/MXene couples is  $\text{Ti}_3\text{AlC}_2/\text{Ti}_3\text{C}_2\text{T}_x$ ,<sup>[12–14]</sup> where the first is usually synthesized from metallic precursors via spark plasma sintering,<sup>[15,16]</sup> hot isostatic pressing,<sup>[17]</sup> or self-propagating high-temperature synthesis,<sup>[18]</sup> while the related MXene is obtained by exposing MAX phase powder to acidic etching. It was demonstrated that the most efficient and fastest etching solution is hydrofluoric acid (HF) at high concentrations. Although other methods have been improved by forming HF in situ by mixing a fluoride salt with other acids or using HF in lower concentrations,<sup>[19,20]</sup> it is necessary to remark that the etching process is still the most problematic step in the MXene production, especially for a potential industrial scaling-up.<sup>[10]</sup> As for the electrochemical characteristics, while the simple  $\text{Ti}_3\text{AlC}_2$  MAX phase has negligible energy storage performances as active electrode material versus Li (it is reported to supply 60 mAh  $\text{g}^{-1}$ <sup>[21]</sup>),  $\text{Ti}_3\text{C}_2\text{T}_x$  MXenes typically show a specific capacity of 150 mAh  $\text{g}^{-1}$  at 260 mA  $\text{g}^{-1}$  and they are capable to sustain long-cycle measurement.<sup>[22–25]</sup> In order to increase even more their performances, an interesting approach that has been proposed recently is the preparation of composites MXene/nanostructures. For its ability to react with significant amounts of lithium ions and its excellent specific capacity performances,  $\text{SnO}_2$  has been extensively employed in the preparation of such composites with  $\text{Ti}_3\text{C}_2\text{T}_x$ . The recent methods for their realization involve atomic layer deposition,<sup>[26]</sup> self-assembly,<sup>[24]</sup> in situ quantum dots and nanoparticles synthesis.<sup>[27,28]</sup> Predictably, all these systems display increased values of specific capacity, ranging from 245 to 620 mAh  $\text{g}^{-1}$  depending on the  $\text{SnO}_2$  percentage and preparation method. However, it should be noted that these chemical approaches generate composites that are structurally unstable to electrochemical reactions with  $\text{Li}^+$ , showing charge efficiencies of less than 99%, as recently demonstrated by our group.<sup>[29]</sup> It should be noted, indeed, that  $\text{SnO}_2$  has a lithiation mechanism consisting of a conversion reaction followed by alloying, and it

suffers from poor cycling stability due to the massive volume change upon charging and discharging.<sup>[30]</sup>

Another strategy to improve the long-term stability of  $\text{SnO}_2$  is to use it with other metal oxides, especially with  $\text{TiO}_2$ . Some works report an increase in the long-cycling through the realization of a  $\text{SnO}_2/\text{TiO}_2$  composite,<sup>[31,32]</sup> whereas other studies highlight the importance of forming an Sn-doped  $\text{Ti}_{(1-y)}\text{Sn}_y\text{O}_2$  rutile system in order to have a reduction in the volume change and a consequent effective long-term stability of the material upon reaction with Li.<sup>[33–36]</sup>

In this work we propose an innovative way to overcome the issues listed before, which has also been independently followed in a recent study on the similar  $\text{Ti}_2\text{SnC}$  MAX system.<sup>[37]</sup> Such a method combines the benefit of avoiding the harmful etching treatment necessary for the MXenes synthesis and is able to generate a new MAX phase-based nanostructured composite material with increased specific capacity with respect to simple MAX and more durable long-term stability upon charging and discharging not only compared to pure  $\text{SnO}_2$  but also to its composites with MXenes.<sup>[29]</sup> Here we report the results on the two Sn-doped  $\text{Ti}_3\text{AlC}_2$  MAX phase systems, synthesized via spark plasma sintering (SPS) with a  $\text{Ti}_3\text{Al}_{(1-x)}\text{Sn}_x\text{C}_2$  formula, with nominal  $x = 0.4$  and  $0.7$ .<sup>[38–40]</sup> These samples have been subsequently subjected to a tailored thermal treatment in air in order to form an external nanostructured layer of oxides (see Figure 1 for a scheme of the process) and avoiding the formation of microstructures and crystallization of undesired phases. The aim is to produce a nanocomposite formed by the unoxidized MAX on the surface of which electrochemically active  $\text{TiO}_2$  and  $\text{SnO}_2$  nanoparticles are generated. The unreacted MAX should act as an electrochemical inactive buffer to preserve the mechanical integrity of the electrode and at the same time improve the electron distribution in the electrode. The pristine MAX phase samples (named  $\text{Ti}_3\text{AlC}_2\text{-RT}$ ,  $\text{Sn}0.4\text{-RT}$ , and  $\text{Sn}0.7\text{-RT}$ ) along with the correspondent oxidized compounds ( $\text{Ti}_3\text{AlC}_2\text{-Ox}$ ,  $\text{Sn}0.4\text{-Ox}$ , and  $\text{Sn}0.7\text{-Ox}$ ) have been characterized, and the latter were directly studied as active materials for negative electrodes in LIBs.

Sn0.4\_Ox and Sn0.7\_Ox present a remarkable specific capacity of 250 and 300 mAh g<sup>-1</sup> and an outstanding mean Coulomb efficiency of 99.62% and 99.64% over 600 cycles at 150 mA g<sup>-1</sup> in half cell; finally, their efficacy as negative electrode has been proved in a full cell configuration versus a LiNi<sub>0.8</sub>Mn<sub>0.1</sub>Co<sub>0.1</sub>O<sub>2</sub> (NMC 811) positive electrode.

A comprehensive investigation of these materials has been carried out: the MAX phases have been preliminarily characterized by X-ray diffraction (XRD), thermal gravimetric analysis (TGA), and scanning electron microscopy (SEM). A subsequent more in-depth analysis by synchrotron X-ray diffraction (SXRD), neutron diffraction (ND), transmission electron microscope (TEM), energy dispersive x-ray spectroscopy by scanning transmission electron microscope (STEM-EDX), Raman spectroscopy, and CHNS was accomplished. All the analyses agree that Sn-doped oxidized MAX phases have a composition that includes a TiO<sub>2</sub>/Ti<sub>(1-y)</sub>Sn<sub>y</sub>O<sub>2</sub> mix that is the true responsible for the good specific capacity and long-cycling stability, making such samples interesting candidates for next-generation LIBs.

## 2. Results and Discussion

### 2.1. Structural and Morphological Characterization

The Ti<sub>3</sub>Al<sub>(1-x)</sub>Sn<sub>x</sub>C<sub>2</sub> MAX phases (x = 0, 0.4, 0.7) were synthesized from metallic precursors by SPS. The amount of Sn in the composites was chosen to explore a large compositional range. The phase with the highest amount of Sn (Ti<sub>3</sub>SnC<sub>2</sub>) was excluded because of the difficulties in obtaining it at a high degree of purity. The SPS systems are designed to heat with very high rates and compress mechanically (in the range of tens of MPa) the powder precursors at the same time, in order to facilitate the reactivity and the homogeneity of the final product; it has been validated as a powerful method to prepare high-pure MAX phase at lower temperature and shorter time compared to a conventional oven. This method for simple Ti<sub>3</sub>AlC<sub>2</sub> has been optimized by Gentile et al.<sup>[13]</sup> and for the present work has been adapted to directly dope the MAX phase with Sn during the synthesis. After the synthesis, the three samples have been milled and the powders were analyzed with a first XRD screening, whose results are shown in Figure S1 (Supporting Information). Each of them is characterized by well-defined diffraction peaks. The Ti<sub>3</sub>AlC<sub>2</sub>\_RT curve is the typical pattern of the MAX phase, as also found by several previous works,<sup>[41–43]</sup> while the Sn0.4\_RT and the Sn0.7\_RT patterns show some slight differences with respect to the undoped phase. It is possible to notice that all the peaks are shifted toward lower angles as the Sn concentration is increased, a behavior that has been previously reported<sup>[39]</sup> and that is in-depth discussed in a later section.

In order to find the best conditions for the thermal treatment, and produce a composite made by MAX/SnO<sub>2</sub>/TiO<sub>2</sub>, the oxidation behavior of the powders was carefully examined by TGA in air flow with a heating rate of 7.5 °C min<sup>-1</sup>, the thermal profiles are displayed in **Figure 2**. The acquired data of the Ti<sub>3</sub>AlC<sub>2</sub> and the doped samples are coherent with previous reports on the thermal oxidative behavior of the undoped<sup>[44]</sup> and Sn-doped MAX phase systems.<sup>[45,46]</sup> The overall oxidations of the

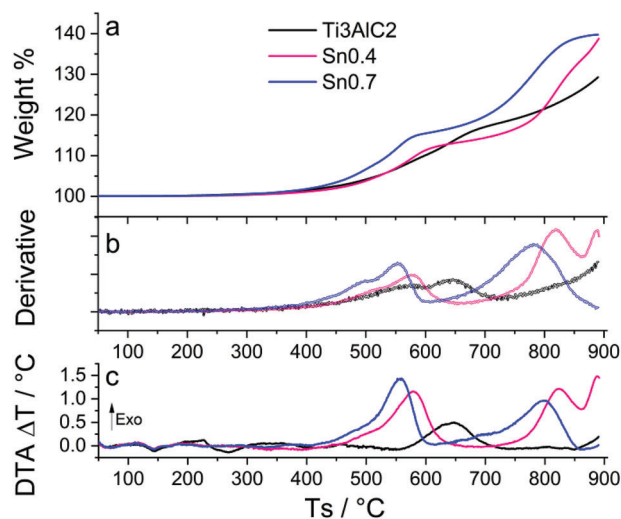
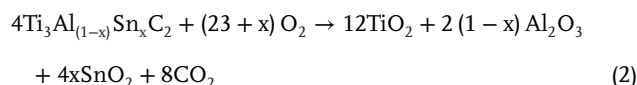


**Figure 2.** Thermal gravimetric analysis (TGA) traces of the MAX phases samples investigated in the temperature range of 30 °C–900 °C: a) weight variation, b) derivative of weight variation, and c) differential thermal analysis.

simple and Sn-doped 312 MAX phases have been rationalized respectively as:



From Figure 2a it can be inferred that for 312 MAX phases the nonisothermal oxidation has two regions marked by a high mass gain rate, which are identified as peaks in the TGA derivative and DTA (Figure 2b,c). For Ti<sub>3</sub>AlC<sub>2</sub> the first oxidation peak is found at 650 °C, while the second is not visible as it should fall at 900 °C. This trend was explained with the following scheme: the first oxidation produces anatase TiO<sub>2</sub>, followed by a transition without a mass increase from anatase TiO<sub>2</sub> to rutile TiO<sub>2</sub>, since it is more thermodynamically stable at a higher temperature, and by the formation of crystalline α-Al<sub>2</sub>O<sub>3</sub> at high temperature.<sup>[45,46]</sup> For the Sn-doped MAX phases the same shape in the TGA profiles is observed. However, with the increase in Sn percentage, these stages shift at lower temperatures, as the DTA peaks corresponding to the first oxidation decrease from 650 °C for Ti<sub>3</sub>AlC<sub>2</sub>, to 580 °C for Sn0.4 and reach 550 °C for Sn0.7. This is a clear evidence that the oxidation resistance of the MAX phase is lowered by the presence of Sn, a behavior that has been reported before.<sup>[45–48]</sup> The oxidation resistance typical of the Ti<sub>3</sub>AlC<sub>2</sub> system has been attributed to the formation of a continuous Al<sub>2</sub>O<sub>3</sub> protective layer on the MAX phase surface, whereas the presence of tin reduces this resistance due to the formation of discontinuity in this layer. For the Sn-doped MAX phases during the first oxidation, the Sn reacts as well and forms a complex variety of mixed Ti/Sn oxides, as inferred from the diffraction data, especially the TEM diffraction patterns, as discussed later. The optimal temperature for the thermal treatment has been determined from the careful

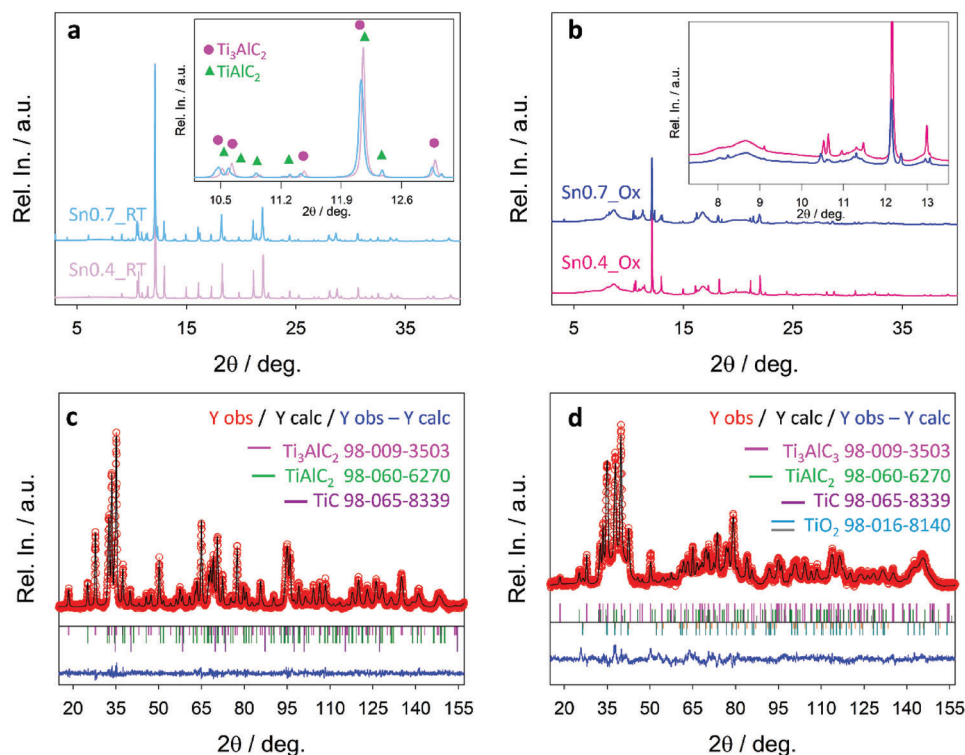


**Figure 3.** Synchrotron X-ray diffraction (XRD) patterns for a) the Sn0.4\_RT and Sn0.7\_RT, b) Sn0.4\_Ox and Sn0.7\_Ox. Rietveld refinement of the neutron pattern data for c) the Sn0.7\_RT sample and d) profile matching analysis for the Sn0.7\_Ox sample.

analysis of these thermal data, with the aim to avoid the formation of crystalline  $\text{Al}_2\text{O}_3$ , obtain only the oxidation of Ti and Sn and preserve a fraction of the MAX phase. For these reasons, the powders were heated up to 600 °C with the same thermal ramp rate used in TGA and were exposed to that temperature for 40 min.

The oxidized samples have been analyzed by XRD, the results are depicted in Figure S1 (Supporting Information). The results of the unoxidized and oxidized samples are here discussed together with the synchrotron and neutron diffraction data for all the compositions, which have been analyzed through the Rietveld refinement and profile matching procedures to determine the complex mixture of phases present in each sample. The results indicated that both as-prepared Sn0.4\_RT and Sn0.7\_RT samples have been successfully prepared with the Sn substitution on the A site. Indeed, the peaks of the 312 MAX phase are clearly visible for both the samples and the 312 MAX phase is the dominant contribution (see **Figure 3a**).

Both the samples contain secondary phases as the 211 MAX phase  $\text{Ti}_2(\text{Al}/\text{Sn})\text{C}$  and TiC, but the phase composition is different. Indeed, the Sn0.4\_RT sample is composed of  $\approx 90\%$  of  $\text{Ti}_3(\text{Al}/\text{Sn})\text{C}_2$ ,  $\approx 9\%$  of  $\text{Ti}_2(\text{Al}/\text{Sn})\text{C}$  MAX phase and a small amount of TiC (see **Table 1** for detailed quantification and **Figure 3c** as an example of the quality of the data). The Sn0.7\_RT sample presents a different phase composition with the amount of the 211 phase increased to  $\approx 20\%$ . The presence of these phases needs to be shortly discussed due to their different nature. The obtaining of highly pure 312 MAX phases belonging to the Al–Sn solid solution is extremely challenging and wide variability in

**Table 1.** Structural parameters for the Sn0.4\_RT and Sn0.7\_RT samples obtained from the analysis of the synchrotron and neutron diffraction data.

	Sn0.4_RT		Sn0.7_RT	
	Synchrotron	Neutron	Synchrotron	Neutron
Phase quantification				
312 [WT%]	92.58 (28)	86.42 (93)	73.34 (27)	78.34 (77)
211 [WT%]	6.71 (6)	13.30 (61)	24.78 (17)	20.62 (43)
TiC [WT%]	0.71 (1)	0.28 (7)	1.87 (2)	1.03 (5)
RWP; CHI2	6.35; 72.7	5.24; 1.46	5.95; 73.0	5.21; 1.15
312 cell parameters				
A [Å]	3.09949 (1)	3.09617 (21)	3.10973 (1)	3.11065 (18)
C [Å]	18.60709 (8)	18.60991(125)	18.612277 (11)	18.61835 (108)
V [Å <sup>3</sup> ]	154.806 (1)	154.499(18)	155.7879 (1)	156.018(15)
Al/Sn [%]	0.57:0.43	0.64:0.36	0.40:0.60	0.43:0.57
211 cell parameters				
A [Å]	3.09557 (7)	3.09705 (29)	3.12162 (2)	3.12129 (18)
C [Å]	13.71374 (31)	13.70163 (200)	13.70214 (12)	13.71171 (123)
V [Å <sup>3</sup> ]	113.807 (5)	113.815 (23)	115.632 (2)	115.689 (14)
Al/Sn [%]	0.62:0.38	0.87:0.13	0.41:0.59	0.35:0.65

the 312/211 ratio and the level of Al/Sn substitution have been reported.<sup>[38,48,49]</sup> Nevertheless, for the specific final application considered in the present study, it must be considered that the 312 and 211 MAX phases have very similar structures and functional properties, thus the presence of a mixture of the two is not

considered detrimental. On the other hand, the eventual presence of TiC impurity can be more problematic, since TiC is the most common impurity obtained during the SPS synthesis of the  $\text{Ti}_3(\text{Al}/\text{Sn})\text{C}_2$  MAX phase and it is undesirable for the final electrochemical properties as it is an insulator.<sup>[13]</sup> Accidentally, the use of Sn as an additive for the synthesis of the  $\text{Ti}_3\text{AlC}_2$  has been previously reported to reduce the thermal explosion during the synthesis of the 312 phase and, as a consequence, to minimize the formation of the TiC.<sup>[38,45,50–52]</sup> The amount of TiC is quantified in less than 1% in both the oxidized Sn doped samples, thus significantly reduced with respect to the typical amount of TiC detected for the  $\text{Ti}_3\text{AlC}_2$  composition synthesized using the same procedure, in good agreement with previous reports on the effect of Sn as additive.<sup>[13,50]</sup>

The refined cell parameters for the 312 phase, reported in Table 1, indicated an expansion of the cell with the increase of the Sn content, coherently with previous literature data as shown in Figure S2 (Supporting Information); this can be expected due to the difference in the Shannon atomic radius (158 and 143 pm for Sn and Al, respectively). The refined values of Al and Sn occupancies are reported in Table 1 and show a good agreement with the nominal composition with higher discrepancy for the Sn0.7\_RT sample. The cell expansion has as a consequence the shift of the MAX phase peaks to lower angles, as clearly visible in Figure S1 (Supporting Information) and Figure 3.

From the evolution of the cell parameters and the refined Al/Sn occupancies, it is possible to infer that also for the 211 phase the Al has been partially substituted with Sn. Indeed, the cell parameters follow the trend obtained considering the available data for the  $\text{Ti}_2\text{AlC}$  and  $\text{Ti}_2\text{SnC}$  end members of the solid solutions.<sup>[49,53–55]</sup>

Globally, the analysis of the diffraction data demonstrates that the Sn0.4\_RT and Sn0.7\_RT samples are composed of more than 98% of MAX, as a mixture of 312 and 211 phases. Both these phases present Sn doping on the Al site, as confirmed by the expansion of the unit cell with the increasing Sn content.

The evolution of the systems with the thermal treatment has been also monitored through diffraction analysis (data reported in Figure 3b and Figure S1, Supporting Information). After the oxidation the reflections of the 312 and 211 phases are still visible and do not shift in any of the three samples, which means that the oxidation involves only a portion of the MAX grains leaving unaltered the rest. For  $\text{Ti}_3\text{AlC}_2\text{-Ox}$ , the appearance of a small amount of anatase and rutile broadened peaks is observed, on the contrary for the Sn-doped composition the intensity of broad reflection associated with these phases is much higher suggesting an increasing content of oxides products with the increasing Sn doping. These broad peaks can be explained by the amorphous/nanoscale formation of mixed Ti/Sn oxides phases with different relative percentages of Ti and Sn.

Although the thermal treatment temperature (600 °C for 40 min) should not lead to the formation of crystalline  $\text{Al}_2\text{O}_3$ , which takes place at around 1000 °C, the presence of amorphous  $\text{Al}_2\text{O}_3$  must be supposed considering the mass balance of the overall oxidation reaction. On the contrary, the appearance of crystalline anatase  $\text{TiO}_2$  and a solid solution oxide in the form  $\text{Ti}_{(1-y)}\text{Sn}_y\text{O}_2$  is observed. This mixed oxide shows a rutile structure and cell parameters that are intermediate between the values reported in literature for rutile  $\text{TiO}_2$  and cassiterite  $\text{SnO}_2$ . Due to the complex-

ity of the experimental patterns, the profile matching procedure was considered for the analysis since phase quantification is not allowed. Nevertheless, from the inspection of diffraction data it is possible to infer that the Sn0.7\_Ox contains a higher amount of oxidized nanostructured products. This can be explained considering the higher amount of 211 phase in the Sn0.7\_RT sample with respect to the Sn0.4\_RT ( $\approx 20\%$  versus  $\approx 9\%$ ) more prone to thermal oxidation. Moreover, the higher content of tin favors thermal degradation, as already discussed in the initial section.

The presence of nanostructures is confirmed also by the SEM analysis, reported in Figure 4. The MAX phase shows the well-known compact lamellar morphology, which is found in both the undoped and Sn-doped samples (Figure 4a,c,e). The appearance of the oxidized samples is quite different for different samples. For  $\text{Ti}_3\text{AlC}_2\text{-Ox}$  it is possible to notice some cracks and grains covered by a homogeneous roughness, whereas in Sn0.4\_Ox and Sn0.7\_Ox there is a plethora of spherical nanostructures that lie regularly in correspondences of the edges of the lamellae. Although the TGA in Figure 2 could suggest that at 600 °C the temperature is barely sufficient for  $\text{Ti}_3\text{AlC}_2$  to start the formation of the granular crystalline  $\text{TiO}_2$ , a TGA executed in air with the same temperature profile as the thermal treatment (see Figure S3, Supporting Information) evidences that this temperature is enough to permit the oxide formation. This is in agreement with a precedent study that has demonstrated that in the range 550–650 °C  $\text{Ti}_3\text{AlC}_2$  has an enhanced oxidation phenomenon due to peculiar kinetics.<sup>[56]</sup> Also, the CHNS results confirm the presence of abundant oxidized products for  $\text{Ti}_3\text{AlC}_2\text{-Ox}$ , as it is further discussed later. The partial oxidation of the MAX phase obtained with the design of an appropriate thermal treatment is confirmed by diffraction and SEM analysis.

The peculiar composition and nanostructure of the oxidized products, presenting cores of conductive MAX phases with Ti/Sn oxides on the surface is even more evident from the TEM analysis reported in Figure 5. The Sn0.4\_Ox and Sn0.7\_Ox samples show a radical change in morphology after the oxidation: before the thermal treatment, the samples have the compact aspect typical of the MAX phase scales, which is coherent with the SEM observations. After the thermal treatment in air, instead, a crust-like morphology is observed (Figure 5e,g). Since the reaction with oxygen proceeds from the outside toward the internal part of each MAX phase grain, it results in an outer layer made of oxide nanostructures in the dimensions range of 10–20 nm (see Figure 5i,l), and in an internal core of unreacted MAX phase. These observations confirm the hypothesis initially proposed on the base of the thermal analysis profiles. The dimension of these nanostructured oxides is consistent with the massive broadening of the corresponding peaks in the diffraction data. The crystal structure of these oxides has been studied also with TEM diffraction, and since this technique has the intrinsic limit of being very local, several spots have been considered (as reported in Figure S4, Supporting Information) and compared to the TEM images of such crystalline nanostructures. The presence of the  $\text{Ti}_{(1-y)}\text{Sn}_y\text{O}_2$  solid solution is especially evident in Sn0.4\_Ox (Figure S4e, Supporting Information). The ability to form a  $\text{Ti}_{(1-y)}\text{Sn}_y\text{O}_2$  solid solution is commonly known and reported by several works, both for anatase<sup>[57]</sup> and especially rutile.<sup>[33,58]</sup> Since Sn has a larger Shannon ionic radius than Ti (55 and 42 pm for  $\text{Sn}^{4+}$  and  $\text{Ti}^{4+}$ , respectively), the substitution of the Sn in the Ti sites causes an

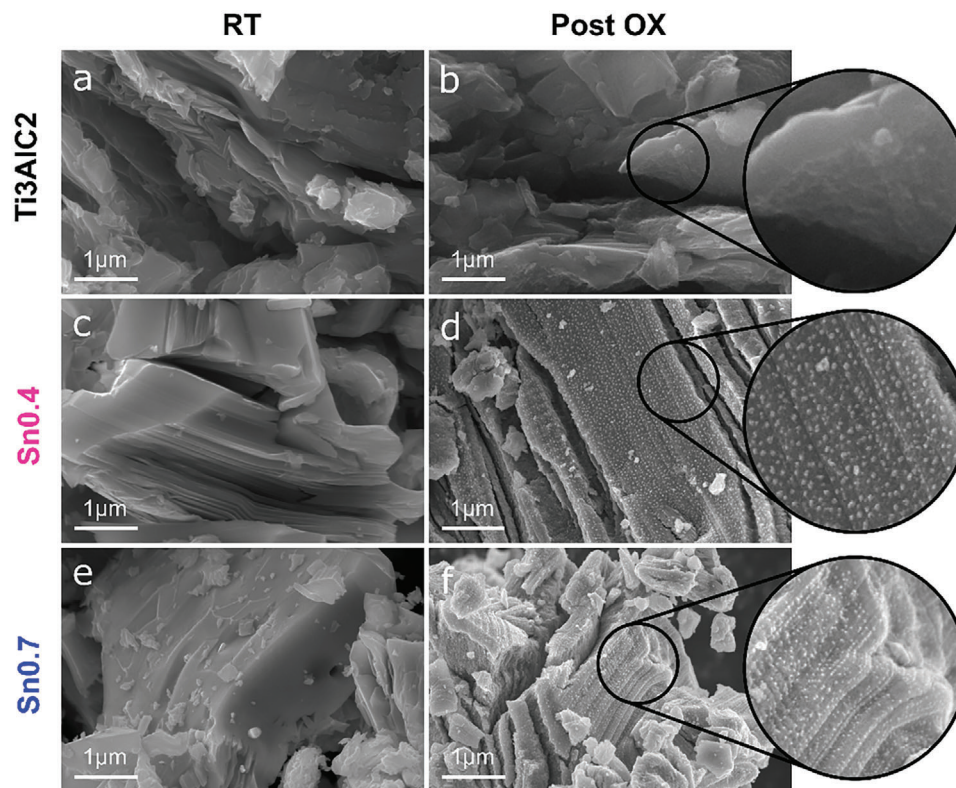


**Figure 4.** Scanning electron microscopy (SEM) images of a) Ti<sub>3</sub>AlC<sub>2</sub>\_RT, b) Ti<sub>3</sub>AlC<sub>2</sub>\_Ox, c) Sn<sub>0.4</sub>\_RT, d) Sn<sub>0.4</sub>\_Ox, e) Sn<sub>0.7</sub>\_RT, and f) Sn<sub>0.7</sub>\_Ox.

expansion of the rutile lattice, shifting the rutile peaks to lower angles in the diffraction patterns.<sup>[58]</sup> This description is coherent with the behavior of the peaks from Sn<sub>0.4</sub>\_Ox (Figure S4e, Supporting Information): they fall in between the SnO<sub>2</sub> and TiO<sub>2</sub> rutile theoretical peaks, having intermediate crystal parameters, as also evident from the analysis of the neutron and synchrotron diffraction data. In order to have more details on the relative percentage of Al and Sn in the Ti<sub>(1-y)</sub>Sn<sub>y</sub>O<sub>2</sub> particles of the Sn<sub>0.4</sub>\_Ox sample, the different profiles e1–e5 reported in Figure S4e (Supporting Information) have been analyzed: for each spot, the  $x$  corresponding to each peak has been derived by linear regression, then the average  $x$  has been calculated among the peaks. The  $y$  substitution in Ti<sub>(1-y)</sub>Sn<sub>y</sub>O<sub>2</sub> is found to be predominantly  $\approx 0.40$  and  $\approx 0.66$  (all the results are summarized in Table S1, Supporting Information). As for Sn<sub>0.7</sub>\_Ox, this particular character is not as clear, but it is evident that an anatase phase is also present.

To further address this aspect, Raman spectroscopy was carried out. The results, in good agreement with the diffraction measurements, are summarized in **Figure 6** and Figure S5 (Supporting Information). Reference spectra of samples before oxidation show the characteristics of the Ti<sub>3</sub>AlC<sub>2</sub> MAX phase represented by a strong mode around 650 and 270 cm<sup>-1</sup><sup>[59]</sup> (Figure S5, Supporting Information) which are attenuated in the spectra of the Sn-based oxidized samples (Figure 6). The attenuation is particularly pronounced in the Ti<sub>3</sub>AlC<sub>2</sub>\_Ox sample as a result of both the presence of surface oxide layers (Figure 4b) and their poor crystallinity (Figure S1, Supporting Information) which widens their signals. In both the Sn-based oxidized samples, the attenu-

ation of the MAX phase signals is due to the strong Raman signal produced by the nanoparticles, which are localized on the surface of the lamellae and masks the MAX phase signals. Indeed, the oxidized samples exhibit Raman spectra characterized mainly by the presence of signals from the rutile and anatase phases of TiO<sub>2</sub>. The intense vibrational modes  $E_g$  and  $A_{1g}$  of rutile (around 440 and 610 cm<sup>-1</sup>, very broad) are present in all samples, while the Eg(1) vibration of anatase (around 148 cm<sup>-1</sup>, sharp peak) is clearly detected in sample Sn<sub>0.7</sub>\_Ox.

Sn-substituted rutile is difficult to detect by Raman<sup>[60]</sup> because SnO<sub>2</sub> and TiO<sub>2</sub> share a common crystal structure and the main Raman modes involve principally oxygen vibrations.<sup>[61]</sup> On the contrary, the Eg(1) mode of anatase involves mainly the Ti vibration and its frequency shift is expected in Sn-substitute crystal.<sup>[61]</sup> Since in the Sn<sub>0.7</sub>\_Ox sample the shift is not observed, we can conclude that Sn does not incorporate into the anatase phase. Finally, the lack of clear evidence of pure SnO<sub>2</sub> Raman modes suggests the presence of a Ti<sub>1-y</sub>Sn<sub>y</sub>O<sub>2</sub> solid solution in the rutile phase.

Last, a CHNS analysis was executed to quantify the presence of carbon in both the unoxidized and oxidized samples. In the pristine samples it further confirms the composition of the materials, while in the oxidized samples, the aim was to have a gross quantification of the amount of MAX phase still present in the powders after the thermal treatment; the results are shown in Table S2 (Supporting Information) and have been interpreted with the following assumptions. First, the percentages of the 312, 211, and TiC phases have been taken from the SXRD refinement (Table 1), due to the best matching with the CHNS data of the

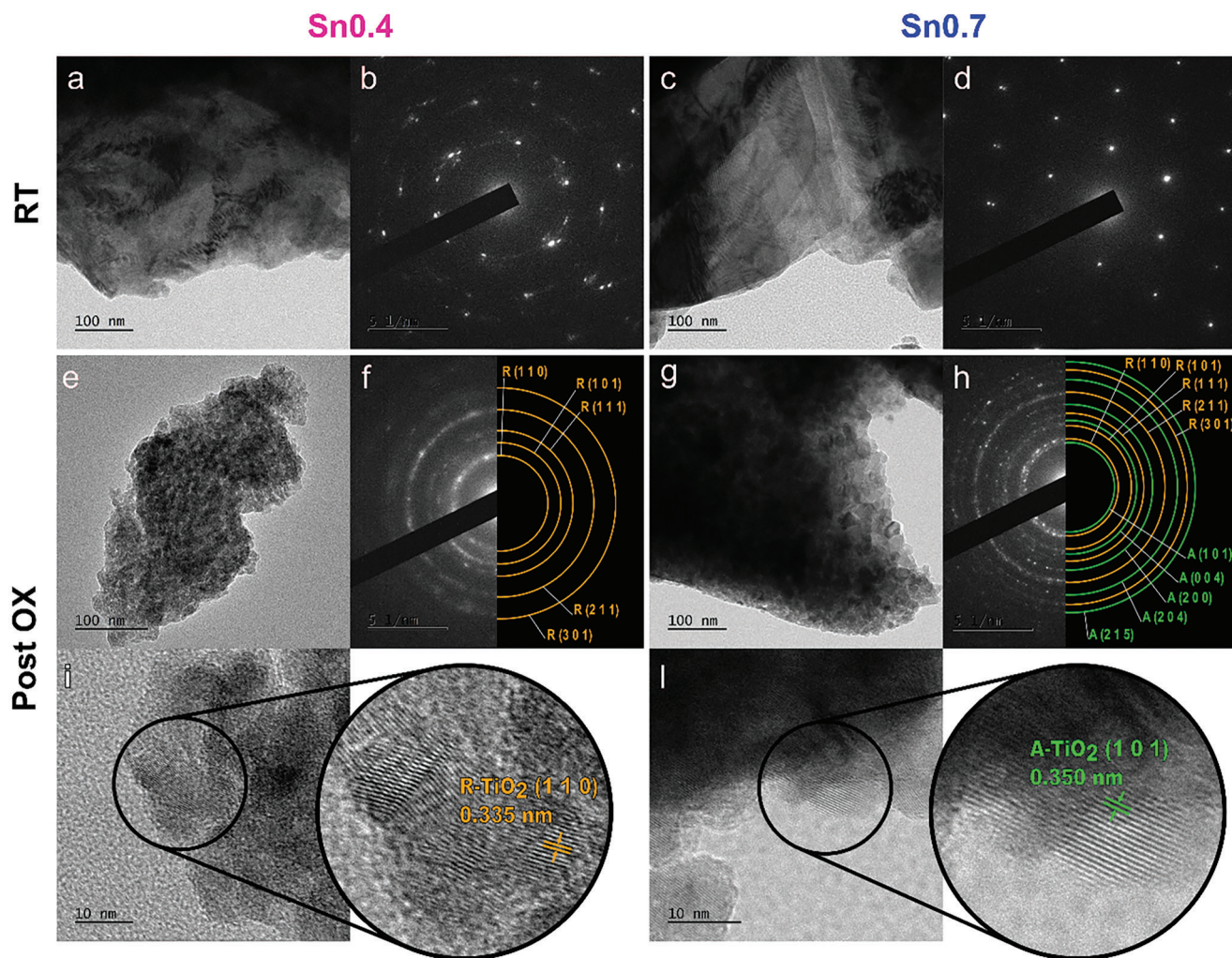


**Figure 5.** Transmission electron microscope (TEM) images of Sn0.4\_RT, and Sn0.7\_RT at low magnification (a,c) with corresponding SAED patterns of the single-crystal MAX phases (b,d). TEM images of Sn0.4\_Ox and Sn0.7\_Ox at low magnification (e,g) with corresponding SEAD patterns of the polycrystalline external oxide structure (f,h), and Sn0.4\_Ox and Sn0.7\_Ox at high magnification (i,l).

unoxidized powders. Then, the reactions considered for the mass balance are the different declinations of Equation (2) (for both 312 and 211 phases, each of them in the case of  $x = 0.4$  and  $0.6$ ). Finally, for the sake of simplicity, the fraction of unreacted material after the oxidation has been considered equal among the three phases, in both Sn0.4\_Ox and Sn0.7\_Ox. The obtained values of MAX phase percentage (taking into account both 312 and 211) are 43.4% and 35.2%, respectively, while the oxides amounts (TiO<sub>2</sub> and Ti<sub>(1-y)</sub>Sn<sub>y</sub>O<sub>2</sub> solution) are found to be 50.7% and 60.2% for Sn0.4\_Ox and Sn0.7\_Ox, respectively. This is consistent with the previous observations: the MAX phase with a higher amount of Sn doping is more prone to oxidation, leading to a larger loss of carbon (CO<sub>2</sub>), which remains only in the MAX. At the same time, the quantity of oxygen reacted is higher for Sn0.7, resulting in a net larger quantity of oxides and a higher weight increase at the end of the oxidation, in agreement with a TGA conducted with the same thermal condition of the thermal treatment (see Figure S3, Supporting Information). Due to the impossibility of refining the complex composition of oxidized species from diffraction

methods, CHNS results were used in explaining electrochemical performance, as is discussed in the following section.

## 2.2. Electrochemical Characterization

Two-electrode coin cells were used to test the electrochemical behavior of the samples as active material in half cells versus metallic Li. In particular, two measurements were carried out, a rate test of 70 cycles, from 15 to 1500 mA g<sup>-1</sup>, and a long cycle test (630 cycles) in which cycles 1–10, 311–320, and 620–630 are performed at 15 mA g<sup>-1</sup> and the others at 150 mA g<sup>-1</sup>. The results are reported in terms of specific capacity, Coulomb efficiency, rate capability, differential capacity, and capacity retention in **Figure 7**. In all cases, the cells need at least 10 cycles at low current to stabilize performance. During the first cycle, the electrodes of Sn0.7\_Ox and Sn0.4\_Ox show an anode capacity of  $410 \pm 3$  and  $347 \pm 2$  mAh g<sup>-1</sup>, respectively, with Coulomb efficiencies of  $57 \pm 1\%$  and  $59 \pm 1\%$ . The low Coulomb

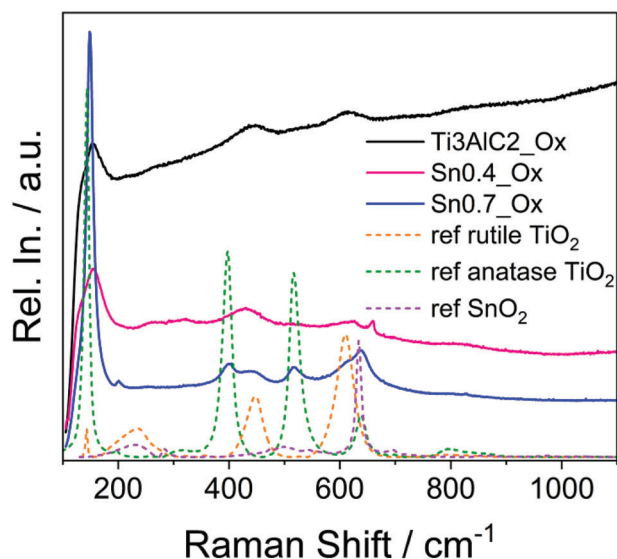
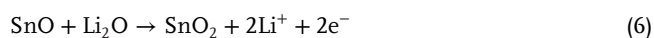


**Figure 6.** Raman analysis of oxidized samples; the rutile  $E_g$  and  $A_g$  vibrational modes are highlighted. The reference plots are taken from the RRUFF Project database (Rutile  $\text{TiO}_2$ : R110109; Anatase  $\text{TiO}_2$ : R060277; Cassiterite  $\text{SnO}_2$ : R040017).

efficiencies can however be mitigated through prelithiation steps, as performed below in the full cell experiment. After 10 cycles at  $15 \text{ mA g}^{-1}$  the specific capacities stabilize at  $343 \pm 5 \text{ mAh g}^{-1}$  ( $\text{Sn0.7\_Ox}$ ) and  $305 \pm 6 \text{ mAh g}^{-1}$  ( $\text{Sn0.4\_Ox}$ ) while the efficiencies increase in both cases to 99.1%. At the same time, the Sn free oxidized sample  $\text{Ti3AlC2\_Ox}$  has much lower capacity (Figure 7b) with a stable value of  $130 \text{ mAh g}^{-1}$ .

These results demonstrate that both the thermal treatment and the Sn-doping are crucial for the use of the MAX phase as good performing electrode material. Since the MAX phase has low capacity when used as negative material per se (all the samples show a specific capacity lower than  $30 \text{ mAh g}^{-1}$  independent from the composition and probably due to the carbon black additive), the real responsible for the good performance of the oxidized samples are the oxides formed with the thermal treatment in synergistic effect with the presence of a conductive core made of MAX phase. The performance trend with the increase in the Sn content is also evident when comparing the differential capacity curves of the first and second cycles for the three oxidized samples (Figure 7c). For  $\text{SnO}_2$  the charge storage reactions can be described as:<sup>[62]</sup>



where  $z$  can be as high as 4.4 giving a theoretical specific capacity of  $783 \text{ mAh g}^{-1}$  for the complete reduction of  $\text{SnO}_2$  to  $\text{Li}_{4.4}\text{Sn}$  (Equations 3 and 4).

The conversion/alloying mechanism leads to the superior specific capacity of  $\text{SnO}_2$  compared to  $\text{TiO}_2$ , which shows, instead,

a  $\text{Li}^+$  intercalation chemistry. The amount of  $\text{Li}^+$  involved in the intercalation ranges from 0 to 1 per unit formula, a value that is strongly dependent on crystal phase, morphology, and facet orientation with a theoretical specific capacity of  $335 \text{ mAh g}^{-1}$  for  $x = 1$ .<sup>[63]</sup> In the  $\text{Ti3AlC2\_Ox}$  sample, the only active material is the  $\text{TiO}_2$ ; the coupled peaks at 1.7 and 2.0 V are related to the lithiation and delithiation of the anatase, which is observed at little percentage, while the reaction with the rutile phase is not recognizable with a defined peak since it is characterized with a continuous slope in the potential profile.<sup>[64]</sup> The behavior of both  $\text{Sn0.4\_Ox}$  and  $\text{Sn0.7\_Ox}$  reported in Figure 7c is similar. During the first cycle reduction peaks are observed at 1.1 V; these peaks are usually correlated to the conversion reaction in Equation (3), however it has been reported that a similar peak can be also found with the first embedding of  $\text{Li}^+$  in a  $\text{Ti}_{(1-y)}\text{Sn}_y\text{O}_2$  solid solution.<sup>[34–36]</sup> At 0.77 and 0.8 V it is possible to observe a shoulder respectively for  $\text{Sn0.4\_Ox}$  and  $\text{Sn0.7\_Ox}$  corresponding to the SEI formation on the oxides grains, and that is shifted to a lower potential for the  $\text{Ti3AlC2\_Ox}$  sample (0.75 V). The following cathodic peaks at about 0.15 V can be ascribed to the alloying of Li with Sn. In the anodic part, the peaks at 0.5 and 1.7 V are related to the dealloying of  $\text{Li}_z\text{Sn}$ , the partial reversible conversion of Sn to  $\text{SnO}_x$ , and/or delithiation of  $\text{TiO}_2$ . For the Sn-doped samples it is possible to notice that during the second cycle the cathodic peak at 1.1 V is not present anymore meaning that such a process is partially irreversible, while a broad peak at 1.5 V appears (for a more distinguishable profile see Figure S7, Supporting Information), which is generally associated with the intercalation reaction with  $\text{TiO}_2$ . The reported differential capacity trends may also be representative of a  $\text{TiO}_2/\text{SnO}_2$  composite, however, as already reported in the XRD, TEM, and Raman analysis there is no evidence of two different peaks for  $\text{TiO}_2$  and  $\text{SnO}_2$  rutile structure.

The rate capability of the samples is very good (Figure 7b), the tin-doped samples are able to sustain a specific capacity useful for practical applications even at  $1.5 \text{ A g}^{-1}$ . In particular, the electrode based on  $\text{Sn0.7\_Ox}$  can deliver 330, 320, 290, 250, 175, and  $125 \text{ mAh g}^{-1}$  at gravimetric currents of 15, 30, 75, 150, 750, and  $1500 \text{ mA g}^{-1}$ , respectively. As reported in Figure 7d, the stability of the Sn-doped samples upon cycling is noticeable, contrary to the behavior of the composites reported in the literature.<sup>[35]</sup> The Coulomb efficiencies of  $\text{Sn0.4\_Ox}$  and  $\text{Sn0.7\_Ox}$  at  $150 \text{ mA g}^{-1}$  have average values of 99.62% ( $\pm 0.4\%$ ) and 99.64% ( $\pm 0.4\%$ ) at  $150 \text{ mA g}^{-1}$  (cycles 100–300), respectively; the capacity retention at  $150 \text{ mA g}^{-1}$  after 620 cycles is about 84% for  $\text{Sn0.4\_Ox}$  and 82% for  $\text{Sn0.7\_Ox}$ . Moreover, by lowering the current value to  $15 \text{ mA g}^{-1}$  for the last 10 cycles (620–630) the  $\text{Sn0.7\_Ox}$  electrode delivered a specific capacity identical to the initial one ( $330 \text{ mAh g}^{-1}$ ).

These electrochemical data can be interpreted through compositional information obtainable from CHNS. Considering only  $\text{TiO}_2$  in the case of  $\text{Ti3AlC2\_Ox}$  and the  $\text{TiO}_2/\text{Ti}_{(1-y)}\text{Sn}_y\text{O}_2$  in the case of the Sn-doped samples as active materials, the theoretical specific capacities of the samples have been calculated considering the compositions extracted from CHNS and reported in Table S2 (Supporting Information). For  $\text{Ti3AlC2\_Ox}$  an intercalation fraction  $x = 0.8$  in  $\text{TiO}_2$  has been used ( $268 \text{ mAh g}^{-1}$  of specific theoretical capacity), and a  $\text{TiO}_2$  percentage of 59.4% has been considered, leading to a theoretical value of  $159 \text{ mAh g}^{-1}$  for



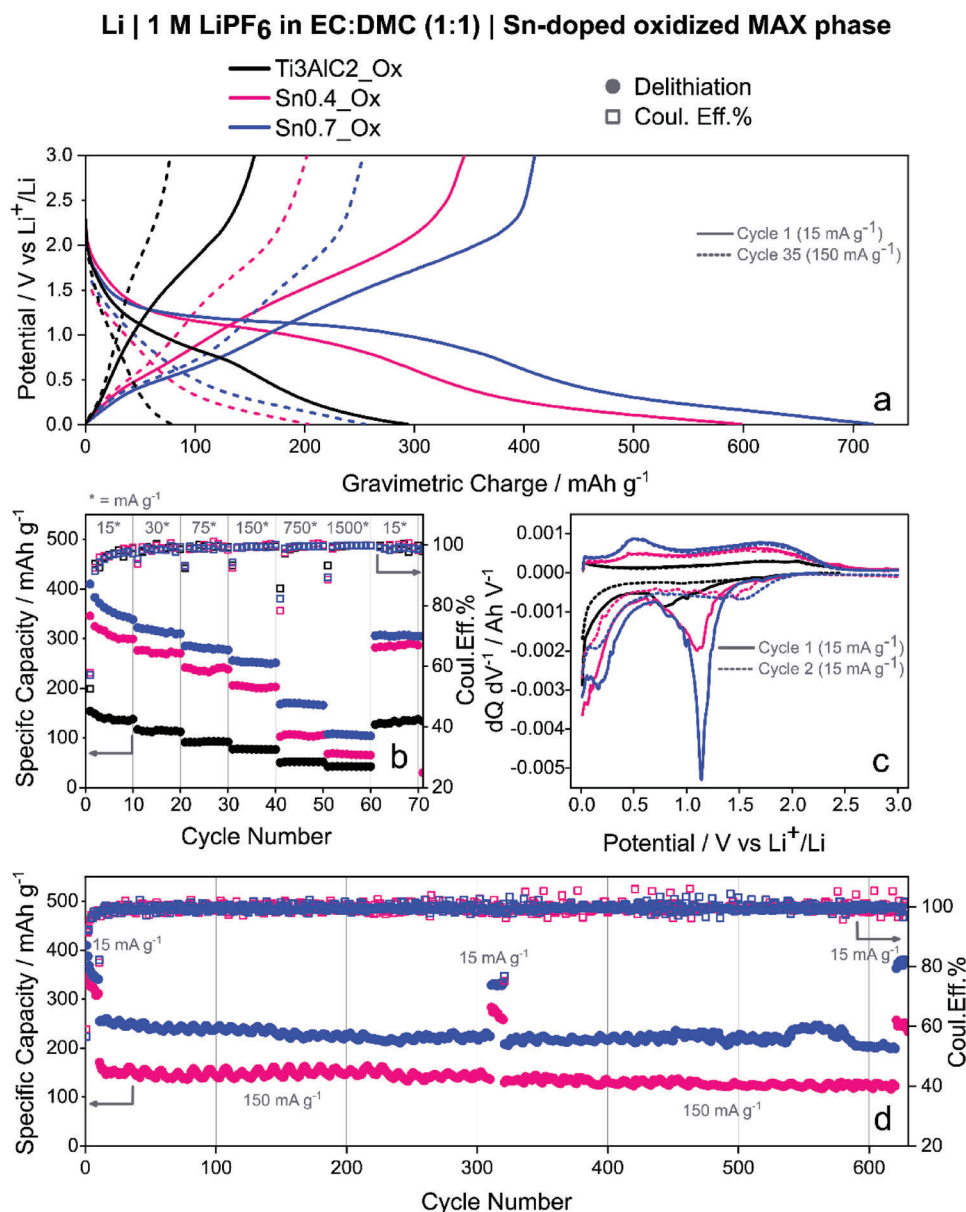


**Figure 7.** a) Charge–discharge potential profiles of Ti<sub>3</sub>AlC<sub>2</sub>O<sub>x</sub>, Sn<sub>0.4</sub>O<sub>x</sub>, and Sn<sub>0.7</sub>O<sub>x</sub> versus Li, cycle 1 and 35. b) Rate test of Ti<sub>3</sub>AlC<sub>2</sub>O<sub>x</sub>, Sn<sub>0.4</sub>O<sub>x</sub> and Sn<sub>0.7</sub>O<sub>x</sub> versus Li. c) Differential capacity of the first and second cycle of Ti<sub>3</sub>AlC<sub>2</sub>O<sub>x</sub>, Sn<sub>0.4</sub>O<sub>x</sub>, and Sn<sub>0.7</sub>O<sub>x</sub> versus Li. d) Long cycling tests of Sn<sub>0.4</sub>O<sub>x</sub> and Sn<sub>0.7</sub>O<sub>x</sub> versus Li.

that specific material (as reported in Table S3, Supporting Information), which is consistent with both the experimental data (see Figure S6, Supporting Information) and previous studies on TiO<sub>2</sub> as negative electrode for LIBs,<sup>[63,65–68]</sup> confirming the validity of the calculations. In the case of Sn<sub>0.4</sub>O<sub>x</sub> and Sn<sub>0.7</sub>O<sub>x</sub>, the contribution of capacity from TiO<sub>2</sub> has been considered in the same way as for Ti<sub>3</sub>AlC<sub>2</sub>O<sub>x</sub>, while for SnO<sub>2</sub> different options have been evaluated. If only Li intercalation in TiO<sub>2</sub> and Li alloying with Sn ( $z = 4.4$ ) are considered, the estimated capacities are way lower than the experimental data (see Figure S6, Supporting Information). This means that at least the conversion of SnO or even SnO<sub>2</sub> (both the reactions show 356 mAh g<sup>-1</sup> of specific theoretical capacity) has to be considered as well. The computed

theoretical values for the two samples are 226 and 313 mAh g<sup>-1</sup> in the first case and 263 and 375 mAh g<sup>-1</sup> in the second case, respectively, for Sn<sub>0.4</sub>O<sub>x</sub> and Sn<sub>0.7</sub>O<sub>x</sub>. The values of experimental mean data at the lowest current are respectively 312 and 360 mAh g<sup>-1</sup>, and especially for Sn<sub>0.4</sub>O<sub>x</sub> it is clear that there are other sources of capacity, such as a pseudocapacitive contribute. All the calculations relative to the theoretical capacities are listed in Table S3 (Supporting Information). To conclude, the differential capacity profiles and the analysis of the specific capacity values support the hypothesis that SnO<sub>x</sub> and TiO<sub>2</sub> are the main active materials in the composite.

The most promising sample, i.e., Sn<sub>0.7</sub>O<sub>x</sub>, has been chosen for the realization of a full cell battery versus NMC 811 in a

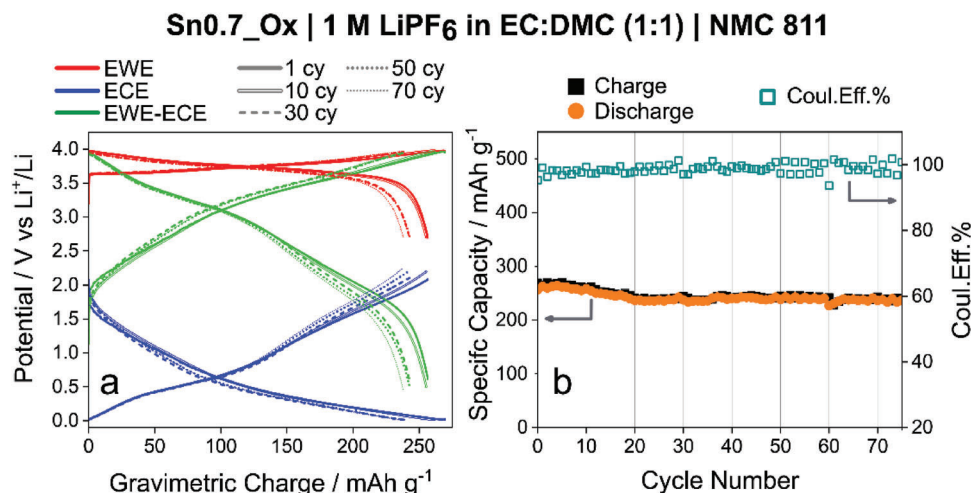


**Figure 8.** a) Charge–discharge potential profiles working electrode (WE, red lines), counter electrode (CE, blue lines), and their difference (WE–CE, green line) of a full cell assembled with Sn0.7\_Ox and NMC 811 as negative and positive electrode, respectively. b) Long-cycling tests of the cell. Gravimetric charges and specific capacities are calculated on the active mass of Sn0.7\_Ox.

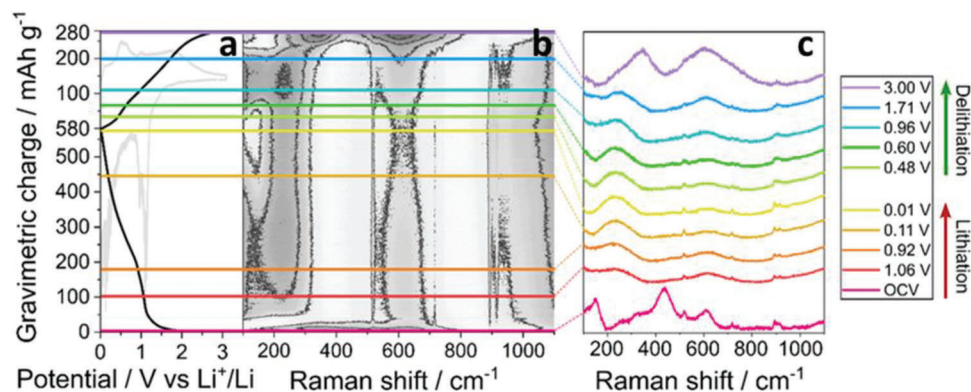


**Figure 9.** a) Charge–discharge potential profiles of Sn0.7\_Ox versus Li, cycle 1 (differential capacity overlapped in light grey). b) Operando Raman spectroscopy map of the sample taken while cycling. c) Raman spectra extracted in correspondence with the differential capacity peaks, highlighted in different colors.

Hohsen cell configuration, whose results are depicted in **Figure 8**. The negative electrode was precycled vs. metallic lithium before the full cell experiment (see details in the Experimental Section). The full cell has shown very good stability, a mean Coulomb efficiency of 98.7% ( $\pm 1.5\%$ ) and a round trip efficiency of 96.3% ( $\pm 1.0\%$ ). Also, it should be pointed out that the full capacity of the MAX phase has not been exploited, since the limiting factor in the cell has been found to be the NMC used as the cathode; therefore, even better performances can be expected with the right capacity balance between anode and cathode masses.

### 2.3. Operando and Postmortem Analysis

In order to have a better understanding of the possible lithiation and delithiation mechanisms, operando Raman measurements have been conducted (first cycle reported in **Figure 9**, and first four cycles reported in Figure S8, Supporting Information). The positions of the peaks in the OCV spectrum are comparable to

those observed for powders (Figure 6, blue curve) but additional signals in the region at wave numbers  $>800\text{ cm}^{-1}$  wherein other components of the electrolyte can contribute. It is worth resuming here that the spectrum is dominated by the Eg(1) vibration of TiO<sub>2</sub> anatase (around  $148\text{ cm}^{-1}$ ), the E<sub>g</sub> and A<sub>1g</sub> of Ti<sub>(1-y)</sub>Sn<sub>y</sub>O<sub>2</sub> rutile (around  $440$  and  $610\text{ cm}^{-1}$ ) and the attenuated signal (shoulder) of the remaining MAX phase.

The spectrum does not change between OCV and 1.2 V, while below this threshold, wherein the conversion reaction is expected to happen, the spectrum suddenly changes showing broad features at  $250$  and  $600\text{ cm}^{-1}$ . These spectral features are maintained for most of the lithiation and delithiation process, except for minor changes. Although neatly attributing these modes to specific vibrations are not straightforward, we can draw some conclusions about the process. Raman modes from substoichiometric tin dioxide SnO<sub>x</sub> ( $x < 2$ ) are expected in the range  $100$ – $300$  and  $400$ – $700\text{ cm}^{-1}$ .<sup>[69]</sup> In particular, peaks at  $238$  and  $245\text{ cm}^{-1}$  are typical of Sn<sub>2</sub>O<sub>3</sub>/Sn<sub>3</sub>O<sub>4</sub> phases,<sup>[70]</sup> while SnO is characterized by strong peaks at  $115$  and  $211\text{ cm}^{-1}$ .<sup>[71,72]</sup> Interestingly

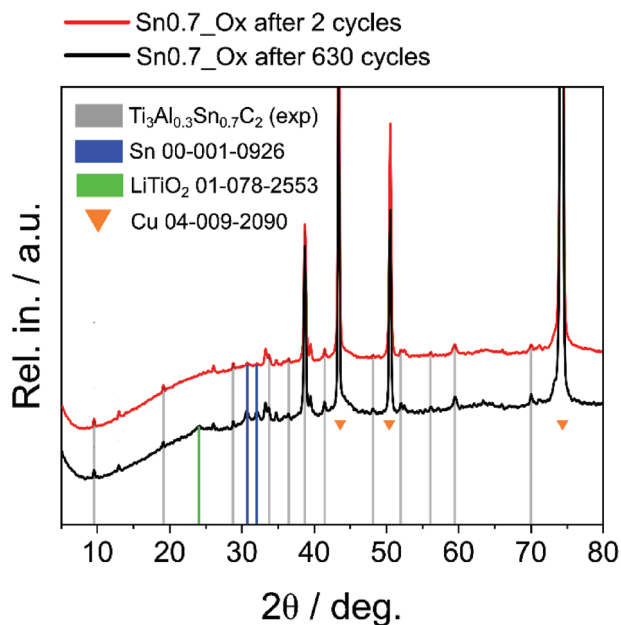


**Figure 10.** X-ray diffraction (XRD) patterns for Sn0.7\_Ox after two cycles (red) and after 630 cycles (black).

all these modes are absent in SnO<sub>2</sub>. Therefore, the broad feature at 250 cm<sup>-1</sup>, which increases slightly during the reduction process, could be attributed to amorphized particles of substoichiometric SnO<sub>x</sub>. The region at 600 cm<sup>-1</sup> is instead typical of both amorphous TiO<sub>2</sub>,<sup>[73]</sup> amorphous SnO<sub>2</sub>,<sup>[74]</sup> and amorphous Sn suboxides.<sup>[75]</sup> At the end of the delithiation process (3.0 V), the spectrum changes further and an additional peak appears at 380 cm<sup>-1</sup> along with a shoulder in the range 500–520 cm<sup>-1</sup>; the latter is in good agreement with the expected position of Li<sub>2</sub>O<sup>[76]</sup> typically observed during lithiation process of oxide electrodes.<sup>[77,78]</sup> More difficult is the interpretation of the signal at 380 cm<sup>-1</sup>, because the reaction products of delithiation (Sn, SnO<sub>x</sub>, Li<sub>2</sub>O, TiO<sub>x</sub>, etc.) are almost transparent in this spectral region. The only significant similarity is with the E<sub>g</sub> vibration modes of nanometric Li<sub>4</sub>Ti<sub>5</sub>O<sub>12</sub>, a well-known material used as a negative electrode in graphite-free lithium batteries.<sup>[79]</sup>

The general amorphization of Sn0.7\_Ox detected by Raman is also confirmed by the XRD measurement acquired on the whole electrode after two cycles in half cell versus metallic Li, as shown in **Figure 10** by the red graph (Cu signals are due to the current collector). It is possible to notice that all the peaks relative to the Ti/Sn oxides are not detected anymore, as previously observed in the operando Raman data. On the other hand, the characteristic peaks of the Sn-doped 312 MAX phase are still visible, confirming that the core MAX phase structure is not subjected to variations upon first cycling. Interestingly, a low-intensity Sn peak can be observed as well. Since all the unreacted Sn found in Sn0.7\_RT is oxidized after the thermal treatment that led it to Sn0.7\_Ox, as shown in Figure S1 (Supporting Information), therefore the Sn found in the cycled Sn0.7\_Ox must be ascribed to the formation of tin from the conversion reaction and its partial irreversibility.

To conclude the study on the presented materials, a post-mortem analysis has been carried out on the Sn0.7\_Ox sample after 630 cycles. The electrode extracted from the half-cell was

subjected to XRD diffraction and later the MAX phase recovered from the electrode was studied with STEM–EDX and TEM. From XRD, a new phase is detected after long cycling (see **Figure 10**): even if broad and not very intense, the peak at 24.3° 2θ could be associated with lithiated titanium oxides.<sup>[80]</sup> The other noticeable feature is the increased amount of Sn, since the peaks associated with Sn are definitely more intense than those in the measurement obtained after two cycles, all other shared peaks being equal.

The morphological, structural, and chemical features of the material after cycling can be observed by TEM diffraction patterns (**Figure S9**, Supporting Information) and in STEM–EDX images (**Figure 11** and **Figure S10**, Supporting Information). Contrary to the EDX data of the uncycled Sn0.7\_Ox powders (**Figure S11**, Supporting Information), where it is possible to observe how the maps of Ti, Al, O, and Sn perfectly fit as expected from the previous TEM images (see **Figure 5g**), in **Figure 11** it is clear that the Sn signal does not fit the others. Indeed, the oxide-coated MAX phase grains can be identified from the corresponding intensities of the EDX signals of Al and Ti (**Figure 11d,e**), because Al is found only in the lamellar structure of the MAX phase, and Ti is found both in the MAX phase cores and in the oxide crusts. Sn, on the other hand, is not only found in the locations just described, it is also more distributed. The C intensities do not provide additional information because the presence of the polymeric binder and carbon black particles is difficult to remove. Thus, despite the low signal of the diffraction peaks, the presence of metallic Sn can be observed also by TEM.

Finally, in **Figure 10** is also possible to notice that the MAX phase core survives unchanged for 630 cycles since the characteristic reflections of the MAX are still present and intense. At the same time, the half-cell does not show signs of failure in 630 cycles as shown in **Figure 7d**, which is quite rare behavior for the systems based on SnO<sub>2</sub>, as they are really unstable upon cycling, and usually show a rapid decay in specific capacity in the first 40–50 cycles.<sup>[31,34,35,81]</sup> Therefore, together with the essential role of the Ti<sub>(1-y)</sub>Sn<sub>y</sub>O<sub>2</sub> solid solution in the capacity retention discussed before, it can be confirmed that the important assist of the MAX phase in guaranteeing the cohesion of the outer oxide crust and the electrical contact is maintained for hundreds of cycles.

### 3. Conclusion

Two Sn-doped MAX phases have been successfully synthesized following the formula Ti<sub>3</sub>Al<sub>(1-x)</sub>Sn<sub>x</sub>C<sub>2</sub> with nominal x content of Sn equal to 0.4 and 0.7. The samples have been subjected to a thermal treatment in air and for the first time have been used as anodic materials in LIB. A TGA study on the pristine powders has confirmed the role of Sn content in the system as responsible for the reduction of the oxidation resistance of the MAX phase, in agreement with the literature,<sup>[46]</sup> and allowed us to carefully design the thermal treatment protocol to avoid formation of crystalline Al<sub>2</sub>O<sub>3</sub>. Through this strategy, we were able to make composites consisting of inert, nonoxidized MAX phase, which acts as a mechanical buffer and improves electronic transport in the electrode, and nanoparticles of Ti/Sn oxides which constitute the active electrode material. The pristine samples present both the 312 and 211 phases in different ratios, constituting >98% of the sample's composition, and diffraction refinement has confirmed

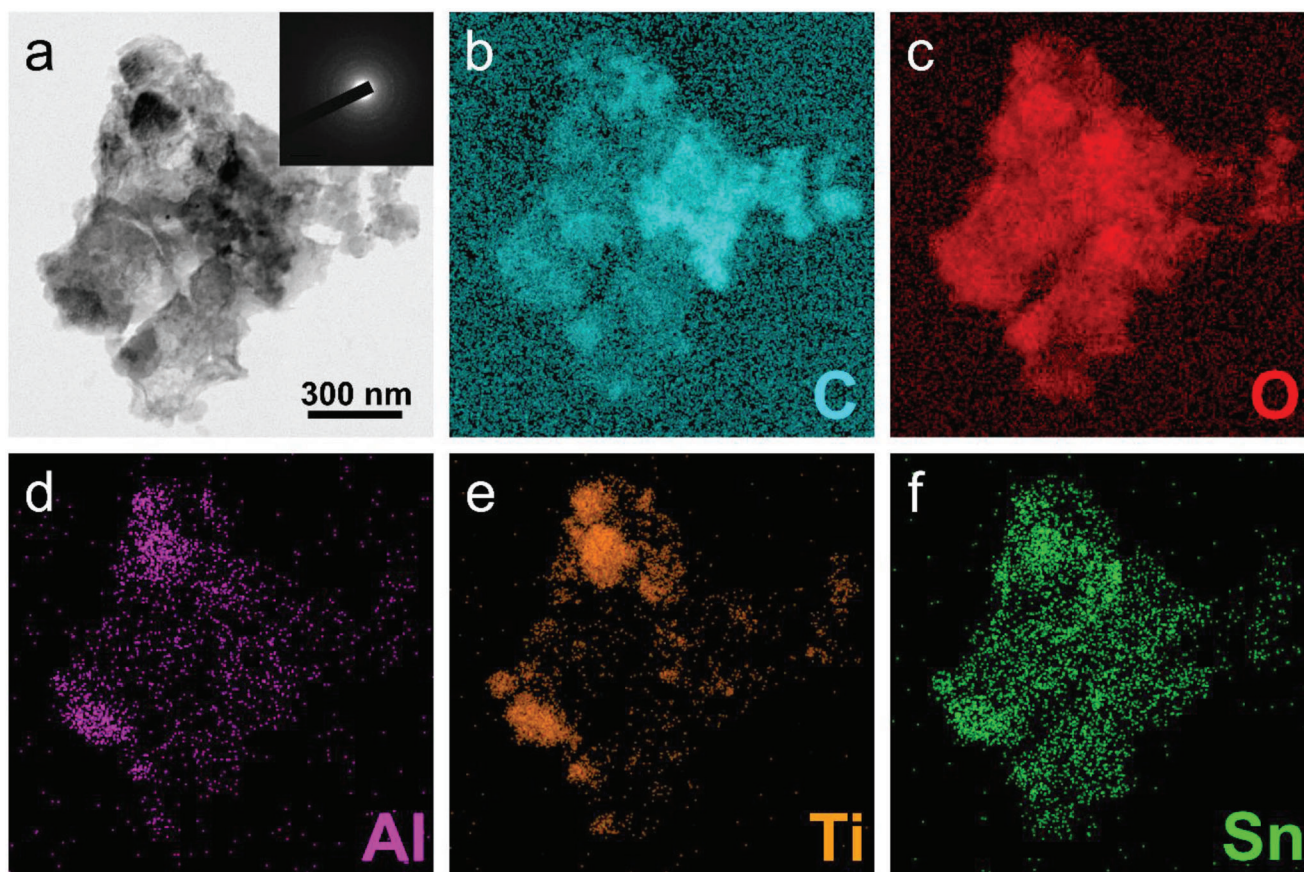


**Figure 11.** a) Transmission electron microscope (TEM) image of Sn0.7\_Ox post 630 cycles (SAED pattern in the inset) with corresponding EDX signal, respectively, of C, O, Al, Ti, and Sn (b–f).

the desired substitution of tin on the aluminum site. The analysis of the thermally treated samples confirms the successful obtaining of the composite system due to the partial 312 and 211 decomposition producing anatase TiO<sub>2</sub> and a rutile Ti<sub>(1-y)</sub>Sn<sub>y</sub>O<sub>2</sub> solid solution with a nanometric structure (around 10–20 nm). These nanostructures have been found to occupy the outer regions of each powder grain, while an intact MAX phase core is present on the inside.

The electrochemical performances are promising, since capacities of 290 and 310 mAh g<sup>-1</sup> have been found respectively for Sn0.4\_Ox and Sn0.7\_Ox, and have been interpreted taking into account the results of the diffraction data and the CHNS analysis, which has helped in determining the effective quantity of active material. The capacities and voltage profiles are consistent with the mass normalization obtainable by CHNS, which is also in agreement with TGA data. The presence of the intact MAX phase core in the grains guarantees good electrical contact as it is highly conductive, moreover, the solid solution of Ti<sub>(1-y)</sub>Sn<sub>y</sub>O<sub>2</sub> hinders the massive volume change typical of pure SnO<sub>2</sub>, which would lead to active material pulverization and loss of capacity after few tens of cycling. The most performant active material, Sn0.7\_Ox, has been employed in a full cell against NMC 811 showing good stability and good efficiency, and postmortem analysis has detected the presence of metallic Sn deriving from SnO<sub>2</sub> conversion upon lithiation confirming this mechanism. Overall,

the role of this MAX core—(Ti/Sn)O<sub>2</sub> nanostructured crust has shown a fundamental effect on the stability of the cells and support in long-life cycling.

#### 4. Experimental Section

**Synthesis of MAX Phase:** The atomic ratios of the precursors Ti/Al/Sn/TiC used to synthesize Ti<sub>3</sub>AlC<sub>2</sub>, Sn0.4, and Sn0.7 were respectively 1:1:0:1.85, 1:0.7:0.4:1.85, and 1:0.4:0.7:1.85. After a shaking treatment in a Turbula mixer for 24 h, 12 g of the precursor powders mix had been put in a graphite die and placed in the chamber of a SPS Dr. Sinter model 925 (Producer Fuji(JP)). With an Ar pressure in the chamber lower than 500 millibars of the atmospheric pressure, the powder mix had been heated up to 1350 °C (heating rate: 80 °C min<sup>-1</sup>) and mechanically compressed up to 30 MPa. After the 30 min long SPS process, the die and the sample had been left cooled at 80 °C and extracted from the chamber. The MAX phase pellets were sandblasted to remove the external crust richer in TiC and then machined with a TiN coated tool to produce the related MAX phase powder.

**Thermal Treatment of MAX Phase:** The MAX phase powders, uniformly distributed in an alumina crucible, were heated in an open tubular oven (Carbolite Gero), with a heating rate of 7.5 °C min<sup>-1</sup> up to 600 °C and a dwell of 40 min at that temperature. No forced air flow was used.

**Thermal Analysis:** The samples were analyzed by TGA (PerkinElmer instrument) with the same heating rate used for the thermal treatment and exploring the temperature range from 30 °C to 900 °C in oxygen flux.

**Materials Diffraction Characterization:** The crystalline phases of the samples were initially evaluated by XRD between  $5^\circ$  and  $80^\circ$   $2\theta$  with a D2 PHASER diffractometer (Bruker AXS) with a copper source ( $\text{Cu-K}_\alpha$ ) with scan step of  $0.02^\circ$  and a scan rate of  $0.02 \text{ s step}^{-1}$ . The experimental data had compared to the reference cards taken from the PDF-4+ 2023 database from International Center for Diffraction Data (ICDD).

Synchrotron XRD data had been acquired at the Swiss Light Source—SLS at the Paul Scherrer Institute.<sup>[82]</sup> Powders were loaded in 0.5 quartz capillaries; the wavelength had been set to  $0.49232 \text{ \AA}$  ( $25.2 \text{ keV}$ ) to avoid absorption effect; data had been collected at room temperature in the  $0.5\text{--}90^\circ$  angular range with step size  $0.036^\circ$ .

Neutron powder diffraction data had been collected at the HRPT diffractometer<sup>[83]</sup> at the Swiss Spallation Neutron Source SINQ in PSI. Powders were loaded in a vanadium sample holder to minimize the background. Samples had been measured at room temperature using  $1.49400 \text{ \AA}$  wavelength in the  $4\text{--}165^\circ$  angular range with step size  $0.05^\circ$ .

The morphology of the samples was characterized by the SEM Zeiss Gemini electron microscope. XRD reference cards were taken from the PDF-4+ 2023 database by ICDD.

**Electrodes Fabrication:** The MAX phase powders were mixed with super P carbon and poly(acrylic acid) (PAA) in the proportion 80:10:10. *N*-methyl-2-pyrrolidone was used as a solvent and the mixture was mixed with an IKA Ultra-Turrax T-50 Homogenizer. The slurry was spread on copper foils for battery cycling versus Li. A thickness of 5 mils ( $127 \mu\text{m}$ ) was obtained using a doctor blade. The films were dried for 12 h at  $120^\circ\text{C}$  in vacuum and calendared. The mass load of active material was around  $1.5\text{--}2 \text{ mg cm}^{-2}$ . For full cell assembly, a commercial cathode of  $\text{LiNi}_{0.8}\text{Mn}_{0.1}\text{Co}_{0.1}\text{O}_2$  (NMC 811, MTI corp.) was used. The cathodic material was mixed, using IKA Ultra-Turrax T-50 Homogenizer, with super P carbon and polyvinylidene fluoride (PVDF), 80:10:10 weight ratio, in *N*-methyl-2-pyrrolidone as solvent. The obtained dispersion was spread on aluminum foil (MTI, thickness 15 mm) with a thickness of 15 mils ( $381 \mu\text{m}$ ) using a doctor blade. The coating was first dried for 12 h under vacuum at  $120^\circ\text{C}$  and then calendared. The mass load of active material was around  $4 \text{ mg cm}^{-2}$ .

**Electrochemical Tests:** The electrochemical performances of the materials were evaluated using a half cell configuration. The CR2032 (MTI) coin cells were assembled in an argon glovebox. The electrodes were cut into 16 mm diameter disks; as electrolyte, commercial LP30 (1 M  $\text{LiPF}_6$  in ethylene carbonate (EC) and dimethyl carbonate (DMC) in 1:1 volume ratio) by MERCK was used; as a separator, a 16 mm in diameter Whatman glassy fiber was employed. The coins were cycled in a multichannel Arbin Lbt21084 at different gravimetric currents applying a standard protocol: 10 cycles at each current (15, 30, 75, 150, 750, and  $1500 \text{ mA g}^{-1}$ ), followed by 10 cycles at the initial current value. Long-term stability tests were executed with the following protocol: 10 cycles at  $15 \text{ mA g}^{-1}$  plus 300 cycles at  $150 \text{ mA g}^{-1}$ , repeated for 1 time. With the addition of 10 cycles at  $15 \text{ mA g}^{-1}$  at the end, it gives a total number of cycles equal to 630. For the full cell, the three electrodes Hohen cell configuration was employed; the cell was assembled using  $\text{Sn}_{0.7}\text{Ox}$  as the negative electrode, NMC 811 as the positive electrode and Li as the reference electrode, LP30 as the electrolyte, and Whatman as a separator. The electrodes were cut into 10 mm diameter disks. The negative material was prelithiated in Hohen (10 cycles at  $15 \text{ mA g}^{-1}$ ) to avoid the loss of capacity at the first cycle due to the SEI formation; the full cell was cycled for 75 cycles at  $0.1 \text{ mA cm}^{-2}$  (i.e.,  $40 \text{ mA g}^{-1}$  referring to  $\text{Sn}_{0.7}\text{Ox}$ ) in the multichannel Bio-Logic VSP-300, using the same GCPL2 technique described in previous work.<sup>[84]</sup>

**TEM Analysis:** The samples had analyzed with the JEOL JEM 2100 Plus operated at 200 kV with imaging and diffraction mode.

**Raman Analysis:** Micro-Raman measurements were carried out by a confocal labRAM (Horiba Jobin-Yvon) spectrometer operating in backscattering configuration and using a helium-neon laser line at  $632.8 \text{ nm}$  as source. The scattered light was detected by a charge coupled device (CCD-Sincerity, JobinYvon). A microscope (Olympus BX40) was used both to focus the excitation on the samples and to collect the scattered light, by a  $100\times$  objective with numerical apertures of 0.95. A neutral filter on the laser line was used to avoid laser-induced sample degradation. The deposited laser power on the sample was kept below  $3 \text{ mW}$  on a spot of about  $2 \mu\text{m}$

in diameter. To minimize the problems induced by the luminescence of the electrolyte, operando measurement had been collected using a solid state laser at  $785 \text{ nm}$  and a long working distance  $50\times$  objective. To limit the degradation of all the component (anode, electrolyte) in the electrochemical cell (model EC-Cell) the laser power had been attenuated up to  $1 \text{ mW}$ . For the operando Raman analysis, the spectra had been collected each 5 min and an autofocus mode had been activated to maximize the Raman signal in the range  $580\text{--}630 \text{ cm}^{-1}$ .

**CHNS Analysis:** The quantities of carbon in the MAX phases were derived by CHNS analysis, with Elementar—vario MACRO cube analyzer.

## Supporting Information

Supporting Information is available from the Wiley Online Library or from the author.

## Acknowledgements

This work was carried out within the MOST - Sustainable Mobility Center and received funding from the European Union Next Generation EU (PI-ANO NAZIONALE DI RIPRESA E RESILIENZA (PNRR) Missione 4 Componente 2, Investimento 1.4 D.D. 1033 17/06/2022, CN00000023). This manuscript reflects only the authors' views and opinion, neither the European Union nor the European Commission can be considered responsible for them. This work has been financed by the Research Fund for the Italian Electrical System under the Three-Year Research Plan 2022–2024 (DM MITE n. 337, 15.09.2022), in compliance with the Decree of April 16th, 2018. This work is partially supported by the SMART-electron Project which has received funding from the European Union's Horizon 2020 Research and Innovation Programme under Grant Agreement No. 964591. This work is partly based on the neutron scattering experiments carried out at the Swiss Spallation Neutron Source SINQ, Paul Scherrer Institute, Villigen, Switzerland.

## Conflict of Interest

The authors declare no conflict of interest.

## Data Availability Statement

The data that support the findings of this study are openly available in ChemRxiv at <https://doi.org/10.26434/chemrxiv-2023-16wxi-v2>, reference number 202316.

## Keywords

composite electrodes, lithium-ion batteries, MAX phase, negative electrodes, tin/titanium oxide

Received: April 15, 2023

Revised: May 14, 2023

Published online:

- [1] J. Lu, Z. Chen, F. Pan, Y. Cui, K. Amine, *Electrochem. Energy Rev.* **2018**, *1*, 35.
- [2] A. Mahmoudzadeh Andwari, A. Pesiridis, S. Rajoo, R. Martinez-Botas, V. Esfahanian, *Renewable Sustainable Energy Rev.* **2017**, *78*, 414.
- [3] F. H. Gandoman, A. Ahmadi, A. M. Sharaf, P. Siano, J. Pou, B. Hredzak, V. G. Agelidis, *Renewable Sustainable Energy Rev.* **2018**, *82*, 502.

- [4] M. Armand, P. Axmann, D. Bresser, M. Copley, K. Edström, C. Ekberg, D. Guyomard, B. Lestriez, P. Novák, M. Petranikova, W. Porcher, S. Trabesinger, M. Wohlfahrt-Mehrens, H. Zhang, *J. Power Sources* **2020**, 479, 228708.
- [5] B. Anasori, M. R. Lukatskaya, Y. Gogotsi, *Nat. Rev. Mater.* **2017**, 2, 16098.
- [6] M. Greaves, S. Barg, M. A. Bissett, *Batteries Supercaps* **2020**, 3, 214.
- [7] C. Ferrara, A. Gentile, S. Marchionna, R. Ruffo, *Curr. Opin. Electrochem.* **2021**, 29, 100764.
- [8] H. Aghamohammadi, R. Eslami-Farsani, E. Castillo-Martinez, *J. Energy Storage* **2022**, 47, 103572.
- [9] L. Verger, C. Xu, V. Natu, H. M. Cheng, W. Ren, M. W. Barsoum, *Curr. Opin. Solid State Mater. Sci.* **2019**, 23, 149.
- [10] M. Alhabeab, K. Maleski, B. Anasori, P. Lelyukh, L. Clark, S. Sin, Y. Gogotsi, *Chem. Mater.* **2017**, 29, 7633.
- [11] M. Sokol, V. Natu, S. Kota, M. W. Barsoum, *Trends Chem.* **2019**, 1, 210.
- [12] D. Er, J. Li, M. Naguib, Y. Gogotsi, V. B. Shenoy, *ACS Appl. Mater. Interfaces* **2014**, 6, 11173.
- [13] A. Gentile, C. Ferrara, S. Tosoni, M. Balordi, S. Marchionna, F. Cernuschi, M. H. Kim, H. W. Lee, R. Ruffo, *Small Methods* **2020**, 4, 2000314.
- [14] D. Xiong, X. Li, Z. Bai, S. Lu, D. Xiong, X. Li, Z. Bai, S. Lu, *Small* **2018**, 14, 1703419.
- [15] W. Zhou, B. Mei, J. Zhu, *Ceram. Int.* **2007**, 33, 1399.
- [16] M. Yunus, R. Kumar, B. C. Maji, M. Krishnan, *J. Eur. Ceram. Soc.* **2022**, 42, 354.
- [17] J. H. Han, S. S. Hwang, D. Lee, S. W. Park, *J. Eur. Ceram. Soc.* **2008**, 28, 979.
- [18] M. Akhlaghi, S. A. Tayebifard, E. Salahi, M. Shahedi Asl, G. Schmidt, *Ceram. Int.* **2018**, 44, 9671.
- [19] C. Peng, P. Wei, X. Chen, Y. Zhang, F. Zhu, Y. Cao, H. Wang, H. Yu, F. Peng, *Ceram. Int.* **2018**, 44, 18886.
- [20] A. Feng, Y. Yu, F. Jiang, Y. Wang, L. Mi, Y. Yu, L. Song, *Ceram. Int.* **2017**, 43, 6322.
- [21] J. Hong, B. Park, *Mater. Lett.* **2023**, 330, 133227.
- [22] D. Sun, M. Wang, Z. Li, G. Fan, L. Z. Fan, A. Zhou, *Electrochem. Commun.* **2014**, 47, 80.
- [23] S. J. Kim, M. Naguib, M. Zhao, C. Zhang, H. T. Jung, M. W. Barsoum, Y. Gogotsi, *Electrochim. Acta* **2015**, 163, 246.
- [24] Y. T. Liu, P. Zhang, N. Sun, B. Anasori, Q. Z. Zhu, H. Liu, Y. Gogotsi, B. Xu, *Adv. Mater.* **2018**, 30, 1707334.
- [25] X. Sun, Y. Liu, J. Zhang, L. Hou, J. Sun, C. Yuan, *Electrochim. Acta* **2019**, 295, 237.
- [26] B. Ahmed, D. H. Anjum, Y. Gogotsi, H. N. Alshareef, *Nano Energy* **2017**, 34, 249.
- [27] J. Xiong, L. Pan, H. Wang, F. Du, Y. Chen, J. Yang, C. (John) Zhang, *Electrochim. Acta* **2018**, 268, 503.
- [28] C. Zhao, Z. Wei, J. Zhang, P. He, X. Huang, X. Duan, D. Jia, Y. Zhou, *J. Alloys Compd.* **2022**, 907, 164428.
- [29] A. Gentile, S. Arnold, C. Ferrara, S. Marchionna, Y. Tang, J. Maibach, C. Kübel, V. Presser, R. Ruffo, *Adv. Mater. Interfaces* **2023**, 10, 2202484.
- [30] Y. Lei, N. Du, W. Liu, H. Wu, D. Yang, *Ionics* **2019**, 25, 4651.
- [31] X. Shi, S. Liu, B. Tang, X. Lin, A. Li, X. Chen, J. Zhou, Z. Ma, H. Song, *Chem. Eng. J.* **2017**, 330, 453.
- [32] T. Autthawong, C. Yodbunork, N. Ratsameetammajak, O. Namsar, Y. Chimupala, T. Sarakonsri, *ACS Appl. Energy Mater.* **2022**, 5, 13829.
- [33] S. Jiao, G. Lian, L. Jing, Z. Xu, Q. Wang, D. Cui, C. P. Wong, *ACS Omega* **2018**, 3, 1329.
- [34] J. H. Um, J. Lim, K. Hengge, C. Scheu, W. S. Yoon, J. K. Lee, Y. E. Sung, *Composites, Part B* **2019**, 166, 613.
- [35] J. K. Ling, C. Karuppiah, M. V. Reddy, B. Pal, C. C. Yang, R. Jose, *J. Mater. Res.* **2021**, 36, 4120.
- [36] H. Liu, N. Li, L. Liu, S. Zhang, J. Wang, K. Chang, Y. Du, W. Zhang, *Composites, Part B* **2022**, 243, 110151.
- [37] S. Jolly, S. Husmann, V. Presser, M. Naguib, *J. Am. Ceram. Soc.* **2023**, 106, 3261.
- [38] S. Dubois, G. P. Bei, C. Tromas, V. Gauthier-Brunet, P. Gadaud, *Int. J. Appl. Ceram. Technol.* **2010**, 7, 719.
- [39] Z. Huang, H. Xu, H. Zhai, Y. Wang, Y. Zhou, *Ceram. Int.* **2015**, 41, 3701.
- [40] G. Bei, B. J. Pedimonte, T. Fey, P. Greil, *J. Am. Ceram. Soc.* **2013**, 96, 1359.
- [41] A. Zhou, C. A. Wang, Y. Hunag, *J. Mater. Sci.* **2003**, 38, 3111.
- [42] K. Goc, W. Prendota, L. Chlubny, T. Strączek, W. Tokarz, P. B. (Chachlowska), K. W. (Chabior), M. M. Bućko, J. Przewoźnik, J. Lis, *Ceram. Int.* **2018**, 44, 18322.
- [43] C. E. Shuck, M. Han, K. Maleski, K. Hantanasirisakul, S. J. Kim, J. Choi, W. E. B. Reil, Y. Gogotsi, *ACS Appl. Nano Mater.* **2019**, 2, 3368.
- [44] X. H. Wang, Y. C. Zhou, *J. Mater. Chem.* **2002**, 12, 2781.
- [45] C. Guo, E. Wang, S. Wang, X. Hou, Z. He, T. Liang, K. C. Chou, *Corros. Sci.* **2021**, 180, 109197.
- [46] C. Guo, E. Wang, Y. Liu, Y. Zheng, T. Yang, X. Hou, *Fundam. Res.* **2022**, 2, 114.
- [47] G. M. Song, Y. T. Pei, W. G. Sloof, S. B. Li, J. T. M. De Hosson, S. van der Zwaag, *Scr. Mater.* **2008**, 58, 13.
- [48] E. Drouelle, V. Brunet, J. Cormier, P. Villechaise, P. Sallot, F. Naimi, F. Bernard, S. Dubois, *J. Am. Ceram. Soc.* **2020**, 103, 1270.
- [49] G. W. Bentzel, M. Naguib, N. J. Lane, S. C. Vogel, V. Presser, S. Dubois, J. Lu, L. Hultman, M. W. Barsoum, E. N. Caspi, *J. Am. Ceram. Soc.* **2016**, 99, 2233.
- [50] N. J. Lane, S. C. Vogel, E. N. Caspi, S. Dubois, V. Gauthier-Brunet, G. P. Bei, M. W. Barsoum, *J. Am. Ceram. Soc.* **2014**, 97, 570.
- [51] A. Mingxing, Z. Hongxiang, Z. Yang, T. Zhaoyun, H. Zhenying, Z. Zhili, L. Shibo, *J. Am. Ceram. Soc.* **2006**, 89, 1114.
- [52] S. Li, W. Xiang, H. Zhai, Y. Zhou, C. Li, Z. Zhang, *Mater. Res. Bull.* **2008**, 43, 2092.
- [53] A. Bouhemadou, *Phys. B: Condens. Matter* **2008**, 403, 2707.
- [54] C. L. Yeh, C. H. Chiang, *Ceram. Int.* **2015**, 41, 6263.
- [55] M. W. Barsoum, G. Yaroschuk, S. Tyagi, *Scr. Mater.* **1997**, 37, 1583.
- [56] X. H. Wang, Y. C. Zhou, *Corros. Sci.* **2003**, 45, 891.
- [57] L. Aldon, P. Kubiak, A. Picard, J. C. Jumas, J. Olivier-Fourcade, *Chem. Mater.* **2006**, 18, 1401.
- [58] R. Bargougui, A. Pichavant, J. F. Hochepped, M. H. Berger, A. Gadri, S. Ammar, *Opt. Mater.* **2016**, 58, 253.
- [59] V. Presser, M. Naguib, L. Chaput, A. Togo, G. Hug, M. W. Barsoum, *J. Raman Spectrosc.* **2012**, 43, 168.
- [60] F. Medjaldi, A. Bouabellou, Y. Bouachiba, A. Taabouche, K. Bouatia, H. Serrar, *Mater. Res. Express* **2020**, 7, 016439.
- [61] O. Frank, M. Zukalova, B. Laskova, J. Kürti, J. Koltai, L. Kavan, *Phys. Chem. Chem. Phys.* **2012**, 14, 14567.
- [62] M. Mirolo, X. Wu, C. A. F. Vaz, P. Novák, M. El Kazzi, *ACS Appl. Mater. Interfaces* **2021**, 13, 2547.
- [63] M. Inaba, Y. Oba, F. Niina, Y. Murota, Y. Ogino, A. Tasaka, K. Hirota, *J. Power Sources* **2009**, 189, 580.
- [64] D. Wang, D. Choi, J. Li, Z. Yang, Z. Nie, R. Kou, D. Hu, C. Wang, L. V. Saraf, J. Zhang, I. A. Aksay, J. Liu, *ACS Nano* **2009**, 3, 907.
- [65] D. Wang, D. Choi, Z. Yang, V. V. Viswanathan, Z. Nie, C. Wang, Y. Song, J. G. Zhang, J. Liu, *Chem. Mater.* **2008**, 20, 3435.
- [66] Y. Zhang, H. Zheng, G. Liu, V. Battaglia, *Electrochim. Acta* **2009**, 54, 4079.
- [67] T. Zeng, P. Ji, X. Hu, G. Li, *RSC Adv.* **2016**, 6, 48530.
- [68] M. Madian, A. Eychmüller, L. Giebler, *Batteries* **2018**, 4, 7.
- [69] B. Eifert, M. Becker, C. T. Reindl, M. Giar, L. Zheng, A. Polity, Y. He, C. Heiliger, P. J. Klar, *Phys. Rev. Mater.* **2017**, 1, 014602.
- [70] F. Wang, X. Zhou, J. Zhou, T. K. Sham, Z. Ding, *J. Phys. Chem. C* **2007**, 111, 18839.
- [71] C. Guillén, J. Herrero, *J. Mater. Sci. Technol.* **2019**, 35, 1706.

- [72] K. J. Saji, Y. P. Venkata Subbaiah, K. Tian, A. Tiwari, *Thin Solid Films* **2016**, 605, 193.
- [73] M. Ocaña, J. V. Garcia-Ramos, C. J. Serna, *J. Am. Ceram. Soc.* **1992**, 75, 2010.
- [74] K. Vijayarangamuthu, S. Rath, *J. Alloys Compd.* **2014**, 610, 706.
- [75] A. Vázquez-López, D. Maestre, J. Ramírez-Castellanos, A. Cremades, *Nanomaterials* **2021**, 11, 976.
- [76] T. Osaka, I. Shindo, *Solid State Commun.* **1984**, 51, 421.
- [77] C. Hu, L. Chen, Y. Hu, A. Chen, L. Chen, H. Jiang, C. Li, *Adv. Mater.* **2021**, 33, 2103558.
- [78] R. Hu, D. Chen, G. Waller, Y. Ouyang, Y. Chen, B. Zhao, B. Rainwater, C. Yang, M. Zhu, M. Liu, *Energy Environ. Sci.* **2016**, 9, 595.
- [79] J. Mosa, M. Aparicio, *Nanomaterials* **2020**, 10, 1369.
- [80] D. H. Lee, B. H. Lee, A. K. Sinha, J. H. Park, M. S. Kim, J. Park, H. Shin, K. S. Lee, Y. E. Sung, T. Hyeon, *J. Am. Chem. Soc.* **2018**, 140, 16676.
- [81] R. Li, W. Xiao, C. Miao, R. Fang, Z. Wang, M. Zhang, *Ceram. Int.* **2019**, 45, 13530.
- [82] P. R. Willmott, D. Meister, S. J. Leake, M. Lange, A. Bergamaschi, M. Böge, M. Calvi, C. Cancellieri, N. Casati, A. Cervellino, Q. Chen, C. David, U. Flechsig, F. Gozzo, B. Henrich, S. Jäggi-Spielmann, B. Jakob, I. Kalichava, P. Karvinen, J. Krempasky, A. Lüdeke, R. Lüscher, S. Maag, C. Quitmann, M. L. Reinle-Schmitt, T. Schmidt, B. Schmitt, A. Streun, I. Vartiainen, M. Vitins, et al., *J. Synchrotron Radiat.* **2013**, 20, 667.
- [83] P. Fischer, G. Frey, M. Koch, M. Konnecke, V. Pomjakushin, J. Schefer, R. Thut, N. Schlumpf, R. Burge, U. Greuter, S. Bondt, E. Berruyer, *Phys. B: Condens. Matter* **2000**, 276, 146.
- [84] C. Ferrara, A. Gentile, S. Marchionna, I. Quinzeni, M. Fracchia, P. Ghigna, S. Pollastri, C. Ritter, G. M. Vanacore, R. Ruffo, *Nano Lett.* **2021**, 21, 8290.